Cell Reports

Article

Periodicity, mixed-mode oscillations, and multiple timescales in a phosphoinositide-Rho GTPase network

Graphical abstract

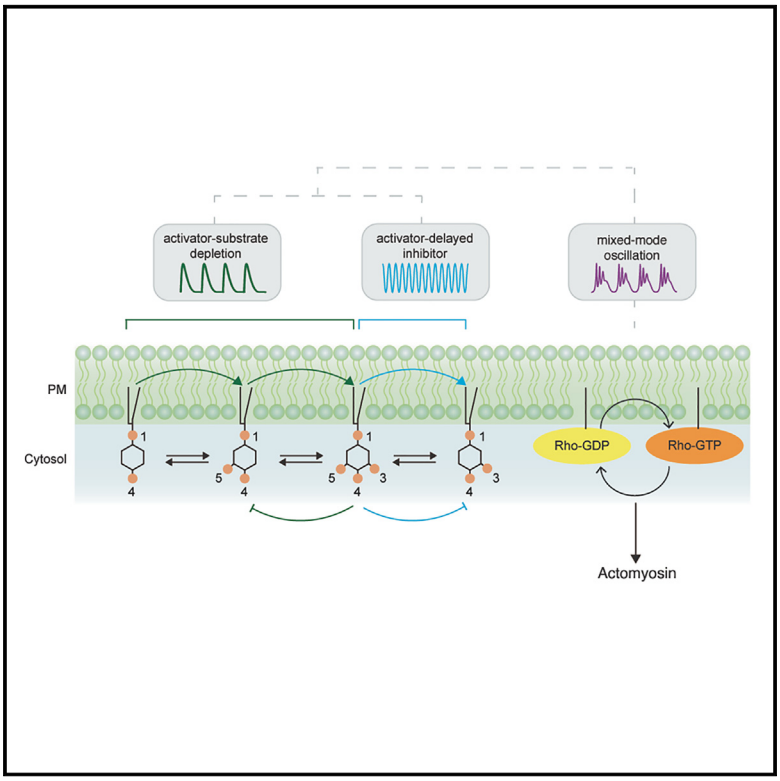

Authors

Chee San Tong, X.J. Xǔ, Min Wu

Correspondence

wu.min@yale.edu

In brief

Tong et al. show that slight modifications to the phosphoinositide metabolism network enable mitotic cells to swiftly transition into different attractor states for cell contractility. Understanding biological systems through these state transitions has broad applicability in the study of signal transduction networks.

Highlights

- Mitotic mast cells show Rho-dependent contractile pulses, enhanced by nocodazole treatment
- Deletion of E-Syt1 or PTEN leads to complex mixed-mode RhoA oscillations
- The slow cycle is regulated by PI(4)P and $PI(4,5)P_2$ via activator-substrate depletion
- The fast cycle is regulated by PIP_3 and $PI(3,4)P_2$ by activator-delayed inhibition

Tong et al., 2023, Cell Reports *42*, 112857
August 29, 2023
https://doi.org/10.1016/j.celrep.2023.112857

CellPress

Cell Reports

CellPress
OPEN ACCESS

Article

Periodicity, mixed-mode oscillations, and multiple timescales in a phosphoinositide-Rho GTPase network

Chee San Tong,[1] X.J. Xǔ,[1,2] and Min Wu[1,3,*]
[1]Department of Cell Biology, Yale University School of Medicine, New Haven, CT 06520, USA
[2]Department of Physics, Yale University, New Haven, CT 06511, USA
[3]Lead contact
*Correspondence: wu.min@yale.edu
https://doi.org/10.1016/j.celrep.2023.112857

SUMMARY

While rhythmic contractile behavior is commonly observed at the cellular cortex, the primary focus has been on excitable or periodic events described by simple activator-delayed inhibitor mechanisms. We show that Rho GTPase activation in nocodazole-treated mitotic cells exhibits both simple oscillations and complex mixed-mode oscillations. Rho oscillations with a 20- to 30-s period are regulated by phosphatidylinositol (3,4,5)-trisphosphate (PIP_3) via an activator-delayed inhibitor mechanism, while a slow reaction with period of minutes is regulated by phosphatidylinositol 4-kinase via an activator-substrate depletion mechanism. Conversion from simple to complex oscillations can be induced by modulating PIP_3 metabolism or altering membrane contact site protein E-Syt1. PTEN depletion results in a period-doubling intermediate, which, like mixed-mode oscillations, is an intermediate state toward chaos. In sum, this system operates at the edge of chaos. Small changes in phosphoinositide metabolism can confer cells with the flexibility to rapidly enter ordered states with different periodicities.

INTRODUCTION

The spatiotemporal regulation of cell contractility is crucial for various morphogenetic events, including cell division. Contractile forces are generated by actomyosin networks, which rely on the activity of myosin II motors to slide antiparallel actin filaments. The assembly of the actomyosin network is governed by the activity of Rho GTPase. In mitosis, Rho plays a critical role in recruiting and assembling components of the cytokinetic ring in animal cells, leading to ring contraction and cell division. Although there is some understanding of how Rho is recruited to the plasma membrane during mitosis, how its recruitment is regulated in mitosis to ensure the fidelity of cell division remains unclear.[1] Waves, pulses, oscillations of contractility, or wandering furrowing activity have been reported for various mitotic cell types, including frog and echinoderm oocytes and embryos,[2–5] *C. elegans* embryos,[6–8] *Dictystelia*,[9] RBL mast cells,[10] and epithelial cells.[11,12] These observations suggest the presence of a nonlinear dynamical network governing Rho dynamics during cell division. This growing body of evidence supports the notion that the contractile machinery involved in cell division comprises local furrowing units capable of assembly, as well as disassembly, pulsation, and oscillation. The coordination of these contractile units is responsible for the formation of productive furrowing, rather than relying solely on a single coherent contractile band acting as a "purse string."[13] Understanding the onset, frequency, duration, amplitude, and coordination of these contractile units and the underlying nonlinear network structure governing such dynamics will thus be fundamental to our understanding of cytokinesis.

Mechanistic understanding of Rho signaling network topology has mostly come from studies of interphase cells where surface contraction pulses or oscillations are also prevalent. The classic model describes contractile pulses by focusing on the mechanical property of the actomyosin network, or the "cytogel," in a manner analogous to how Hodgkin-Huxley equations describe action potential with a single measurement of membrane potential.[14] These models were inspired by works on model systems of large sizes such as the true slime mold *Physarum polycephalum* where cycles of cytoskeletal expansion and contraction can be readily observed and mechanical properties can be measured.[15] Actomyosin-centric mechanical models were also supported by recent experimental work.[16,17] However, information on the chemical state of the "cytogel," also an essential ingredient in the mechanochemical model, is largely absent. Probing the chemical state of the system only became possible in recent years with fluorescent reporters to directly visualize Rho and its interaction networks.[4,18,19] With quantitative investigation of the behavior of RhoA together with actomyosin networks in the contractile pulses and experimental perturbation to these patterns, an emerging view is that there should be a signaling network corresponding to cycles of Rho GTPase activity that acts upstream of myosin II and drive cycles of contraction.[8,18–20]

The generic principle of oscillations requires the interplay of a local self-enhancement activator and an antagonistic effect that decreases production of activator or increases its degradation.[21,22] In the context of Rho activation, inhibitory mechanisms play a crucial role in controlling the onset and duration of Rho activity, thereby influencing the frequency, oscillation period, and refractory phase of Rho pulsing. Previous studies have proposed that Rho guanine nucleotide exchange factors (RhoGEFs) and Rho GTPase-activating proteins (RhoGAPs) could function as the activator and inhibitor, respectively.[2,7,18] In particular, experiments manipulating RhoGAP RGA-3/4 in *Xenopus* oocytes led to a dose-dependent decrease in oscillation period from 150–250 to 50–100 s.[2] However, even in experimental systems that exhibit regular oscillations, the oscillation periods can vary significantly within a single system and between different systems. Reported oscillation periods range from 80 to 120 s in activated frog eggs,[4] 50 to 120 s in starfish oocytes,[5] and 30 to 50 s in U2OS cells.[18] In addition, multiple harmonics have been reported in *Physarum polycephalum*.[23] Therefore, the antagonistic interactions mediated by RhoGEFs and RhoGAPs alone do not adequately explain the observed variability in oscillation timescales or how this variability arises without altering protein expression levels.

Many of the components in the Rho/RhoGEF/GAP network can be recruited to plasma membrane through their binding to phosphoinositide.[24–27] Interestingly, both RhoGEFs[24,26] and RhoGAP[25] have been found to bind to phosphatidylinositol 4,5-bisphosphate ($PI(4,5)P_2$), raising questions about how phosphoinositides specifically influence Rho signaling. While oscillations of various phosphoinositides have been observed in several single-cell systems,[28–36] it remains unknown whether phosphoinositide oscillations could act as a pacemaker for Rho oscillations. Phosphoinositides are widely recognized as key signaling molecules that broadly impact all aspects of cell physiology.[37,38] Different species of phosphoinositide are connected by phosphoinositide kinases and phosphatases, generating a metabolic network that is intriguing from a dynamical systems perspective. The coupling of metabolic reactions in series or in parallel can lead to a significantly expanded range of dynamic behaviors compared to uncoupled systems. For instance, coupling two allosteric enzymes in a flow system, where the product of one enzyme serves as the substrate for the other,[39,40] or having two enzymes catalyzing the same metabolic reaction but with different kinetics,[41] can result in complex oscillatory phenomena such as bursting or deterministic chaos. These dynamical phenomena arise through the coupling of two or more instability-generating mechanisms.[42,43] Although complex oscillations have been modeled in theory[39,40,44,45] and extensively studied in chemical and enzymatic reactions in the 1970s–90s, including Belousov-Zhabotinskii reaction[46,47] and peroxidase-oxidase reaction,[48,49] their presence in cellular systems has been less explored.[50–52]

In this paper, we show that Rho oscillations in nocodazole-treated mitotic rat basophilic leukemia (RBL) cells exhibit periodicity ranging from 30 s to 5 min, which covers periodicities for contractile pulses reported in all experimental systems. We found that the heterogeneity in oscillation frequency is not achieved by a single instability-generating mechanism but requires at least two layers of controls operating at different timescales. We also demonstrate that phosphoinositide metabolism critically controls the timescales for each layer, and coupling of two feedback loops generates complex oscillation dynamics such as period doubling and mixed-mode oscillations. These findings significantly contribute to our understanding of the diverse dynamical behaviors generated by the phosphoinositide-Rho GTPase network and provide an experimental framework for investigating heterogeneity in contractile instability and signal transduction processes in general.

RESULTS

Single-cell variability of Rho oscillations in nocodazole-treated mitotic RBL cells

To understand the molecular network that controls cell contractility, we looked for experimental conditions that allowed us to generate and perturb Rho oscillations. Oscillators convey systems-level characteristics that are informative for dissecting the full topology of the reaction network.[53] To detect the activity of Rho, we employed the use of the rhotekin G protein binding domain (rGBD). The rGBD selectively binds to active Rho (RhoGTP) and undergoes translocation to the plasma membrane upon binding. This translocation can be observed as an increase in fluorescence intensity, which was visualized using total internal reflection fluorescence (TIRF) microscopy. In RBL cells, we found oscillation of Rho dynamics was the most robust when nocodazole, a microtubule depolymerization drug, was introduced to mitotic cells (n = 29 experiments, 57/70 cells). The effect of microtubule poison on contractility was known in the literature, likely indicating that microtubules have a global inhibitory effect on contractility.[54,55] Rho oscillations in mitotic cells are heterogeneous and showed variations both in their periodicities and pulse durations (Figures 1A–1D). Based on fast Fourier transform (FFT), the major period of these oscillations varied from ~30 s to 5 min. The fastest Rho oscillations around 30 s were rare (8/57 cells) (Figure 1A). Most Rho oscillations have lower periodicities (70–180 s) (44/57 cells) (Figures 1B and 1C). Despite the differences in periodicities, the profile of individual Rho pulses has very similar rise phases. When we aligned the peaks of individual oscillatory cycles with different frequencies, it is evident that the rate of Rho recruitment in all three types of simple Rho oscillations is similar and can be superimposed (Figure 1E). The fastest oscillation has a symmetrical rise (~16–20 s) and fall phases (~16 -20s) (Figure 1A), while Rho oscillations with period of ~120 s have similar rise phases but slower decay phase (~36–44 s) (Figure 1B). Duration of the peak does not linearly correlate with oscillation period, as oscillation with a similar period of ~150 s can have very different durations as seen from both autocorrelation analysis and the rise/decay phase of averaged profiles (compare Figures 1B and 1C).

The heterogeneous oscillation periods and pulse durations make it challenging to identify the negative regulators responsible for controlling these parameters because any conclusions would require large sample sizes for statistical confidence. We therefore took an alternative approach. We noticed that besides simple oscillations, complex mixed-mode Rho oscillations were occasionally observed (Figure 1D). Mixed-mode oscillations

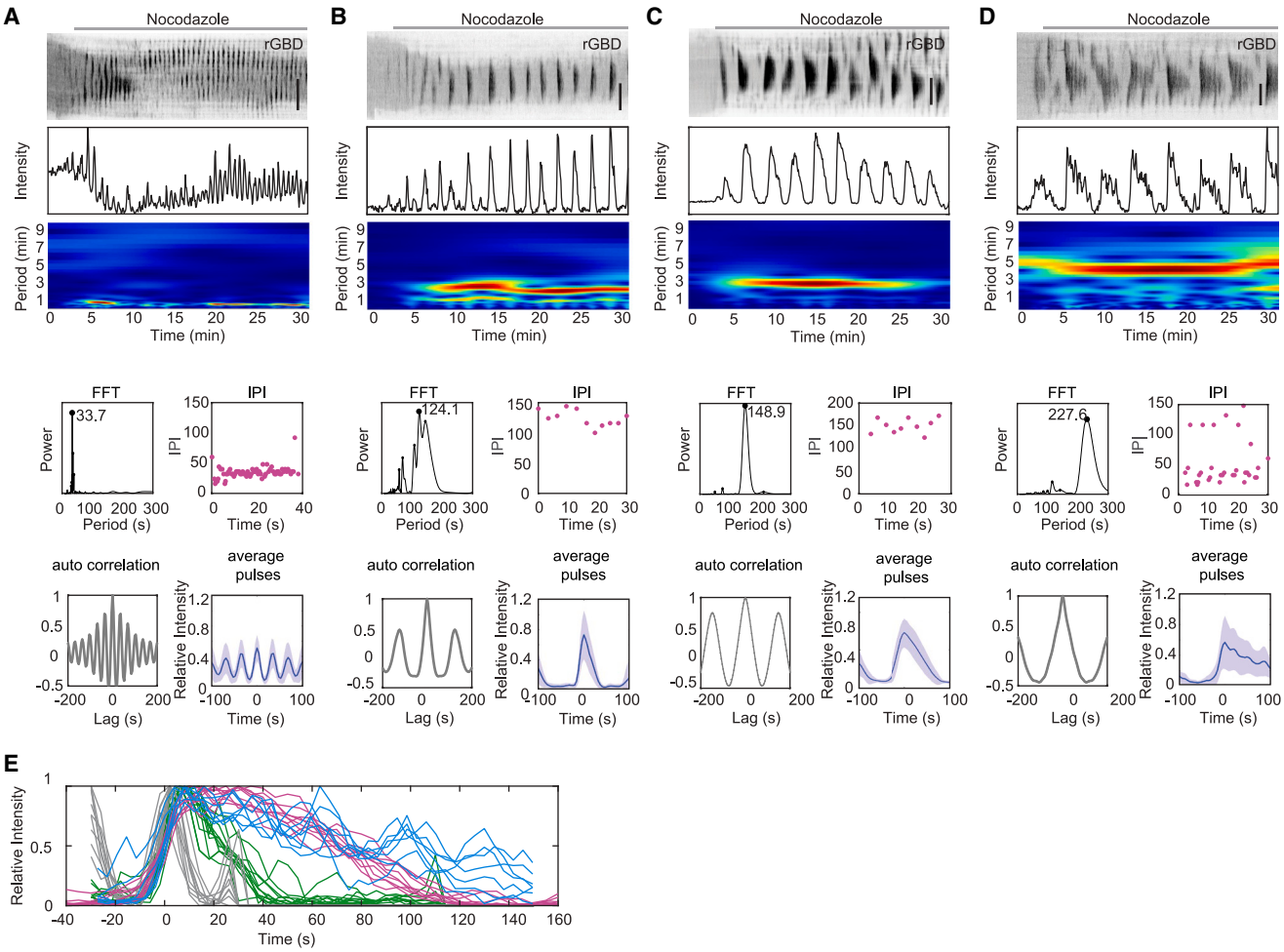

Figure 1. Simple and complex Rho oscillations in nocodazole-treated mitotic RBL cells

(A–D) Top: kymographs, intensity profiles, and wavelet analyses of representative movies depicting simple and complex Rho oscillations in wild-type (WT) cells, visualized using the Rho sensor (rGBD). Bottom: analysis of Rho oscillation properties. Fast Fourier transform (FFT) analysis reveals the major period. Interpeak intervals (IPIs) of the representative movies are plotted against time changes. (A), (B), and (C) display a single interpeak interval, while (D) exhibits two distinct interpeak intervals. Autocorrelation of Rho oscillation signals indicates peak duration. Average profiles of aligned peaks demonstrate the rise and drop phases of an average pulse's intensity profiles. The solid lines represent the mean intensities of the profiles, while the shaded region represents the standard deviations of the intensities.

(E) Alignment of individual peak traces of Rho oscillations, with colors representing different traces: (A) in gray, (B) in green, (C) in magenta, and (D) in cyan. Vertical scale bar: 10 μm.

have oscillatory cycles that consist of large-amplitude oscillations intercalated with small-amplitude oscillations.[56] While FFT of these complex oscillations also gives rise to a single major period around 5 min, interpeak interval analysis reveals two populations of the intervals, centered around approximately 120 s for larger gaps and 30 s for the "nested" peaks (Figure 1D). Complex oscillations arise when there are at least two instability-generating mechanisms. Investigating how these mechanisms are coupled can reveal information on the structure of a higher dimensional network. We therefore chose to understand how complex oscillation patterns arise by looking for experimental perturbations that could increase the occurrence of such events, instead of perturbations that change the distribution of oscillation frequencies.

Phosphoinositide metabolism shifts dynamical regimes of simple and complex oscillations in Rho signaling

Phosphoinositide metabolism plays an important role in recruiting regulators of Rho signaling cascade to plasma membrane. We systematically knocked down major phosphatases involved in the phosphoinositide metabolism (Figure 2A) and scored for percentage of oscillations that exhibit complex oscillation patterns (Figures 2B and 2C). In wild-type (WT) cells, these complex patterns are rare (5/57 cells), and a majority of cells imaged presented simple Rho oscillation (Figure 2D). Hence any condition that leads to frequent appearance of complex pattern would be significant. We observed a significant increase in mixed-mode Rho oscillations in cells with knockdown (KD) of PTEN, a 3-phosphatase that catalyzes the dephosphorylation of the 3′

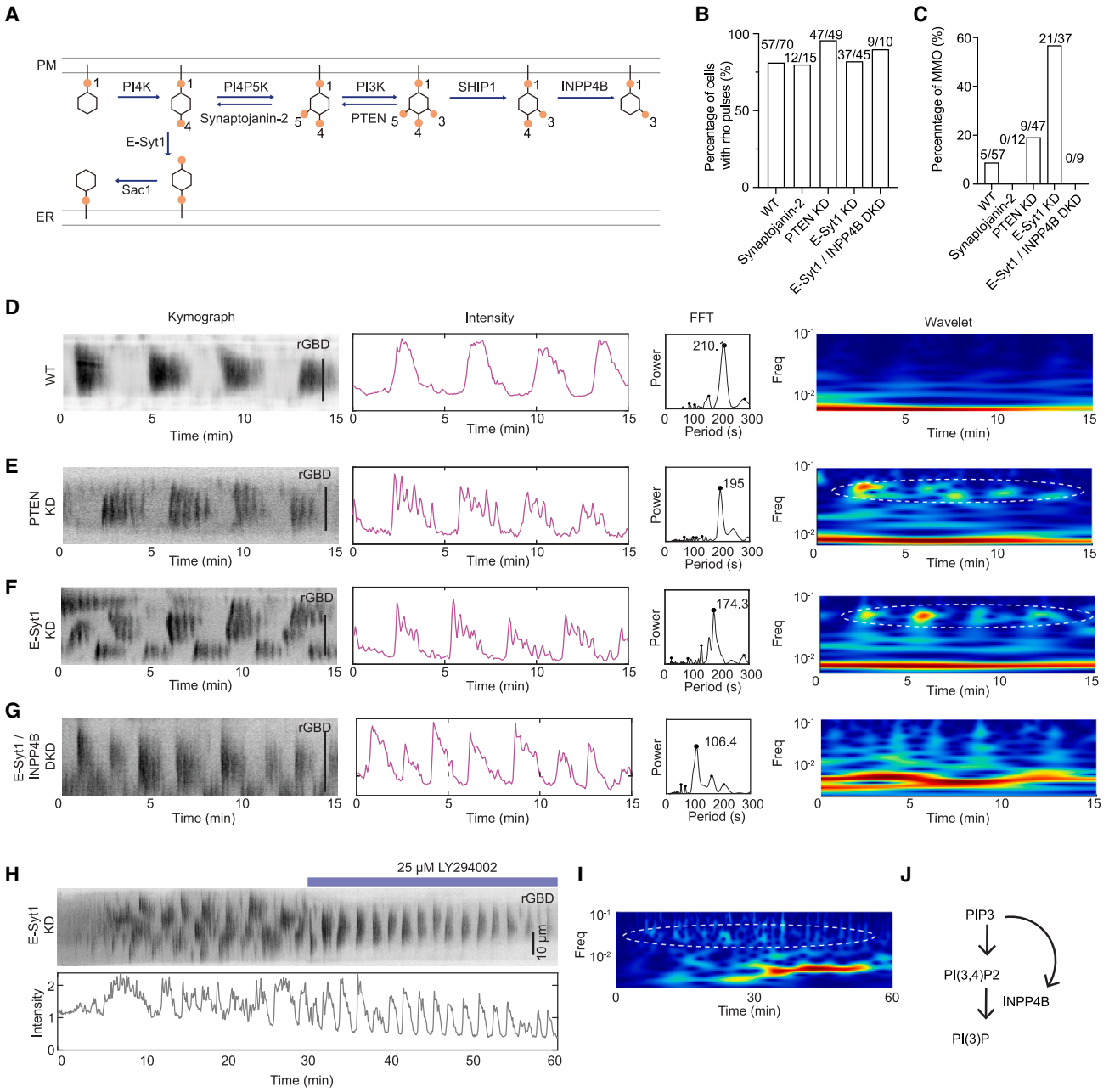

Figure 2. Complex mixed-mode Rho oscillations in PTEN or E-Syt1 knockdown cells

(A) Schematic depicting the phosphoinositide metabolism pathways.

(B) Bar plot displaying the percentage of cells exhibiting Rho oscillations following nocodazole addition.

(C) Bar plot indicating the percentage of cells displaying mixed-mode Rho oscillations under different conditions: wild-type cells (5/57 cells), Synaptojanin-2 KD (0/15 cells), PTEN KD (9/45 cells), and E-Syt1 KD (21/45 cells).

(D–G) Representative kymographs, intensity profiles, FFT, and wavelet analyses of Rho oscillations in WT cells, PTEN KD cells, E-Syt1 KD cells, and E-Syt1/INPP4B double KD (DKD) cells. High-frequency peaks observed in PTEN KD and E-Syt1 KD cells, as shown by wavelet analyses, are indicated by dotted circles.

(H) Representative kymographs and intensity profile of Rho oscillations in E-Syt1 KD cells treated with LY294002.

(I) Wavelet analysis of E-Syt1 KD cells treated with LY294002. Dotted lines represent high-frequency peaks that disappear upon LY294002 addition.

(J) Schematic representation of the fast oscillation circuit. Vertical scale bars: 10 μm.

phosphate of phosphatidylinositol (3,4,5)-trisphosphate (PIP_3) to yield PI(4,5)P_2, but not with KD of Synaptojanin-2, which catalyzes the dephosphorylation of the 5′ phosphate of PI(4,5)P_2 to yield PI(4)P (PTEN KD: 17 experiments, 9/47 cells [19%]; Synaptojanin-2 KD: 5 experiments, 0/12 cells [0%]) (Figure 2C). The most dramatic increase in complex oscillations occurs

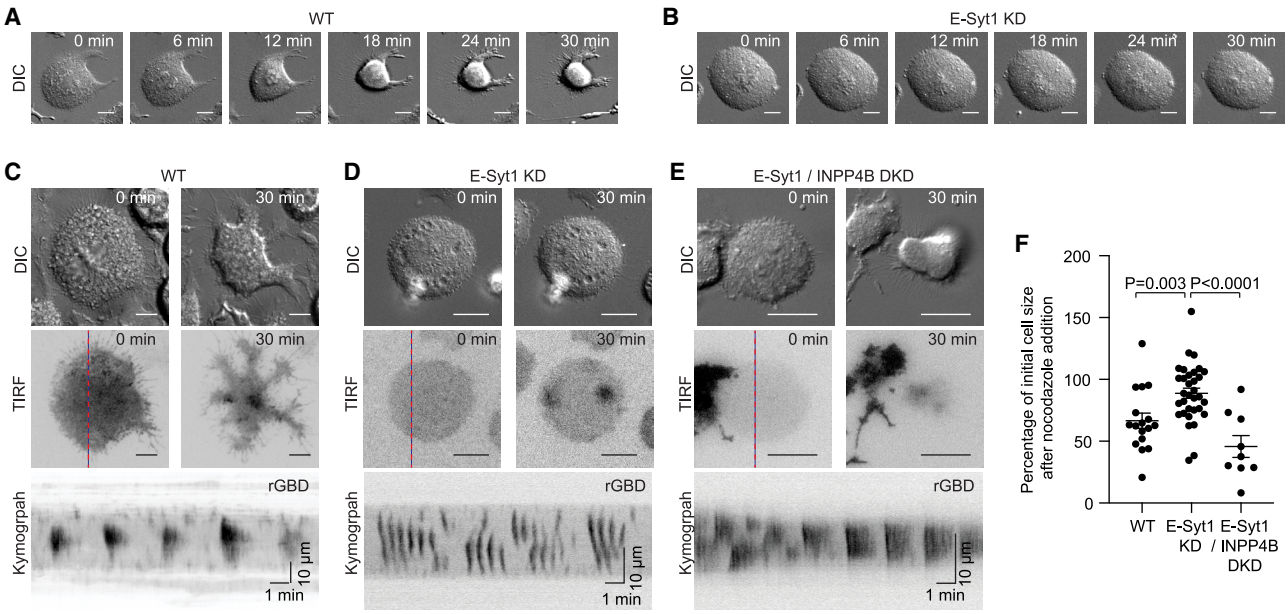

Figure 3. Correlation between oscillation modes and cell contractile behaviors

(A) DIC monographs of a wild-type cell at 6-min intervals after nocodazole addition.

(B) DIC monographs of an E-Syt1 KD cell at 6-min intervals after nocodazole addition.

(C–E) Top and middle: DIC and TIRF monographs of wild-type, E-Syt1 KD, and E-Syt1/INPP4B double KD (DKD) cells at 0 min and 30 min after nocodazole addition. Dotted red lines indicate where kymographs are plotted. Bottom: kymograph of rGBD oscillations in wild-type, E-Syt1 KD, and E-Syt1/INPP4B DKD cells.

(F) Plot comparing size changes of wild-type (n = 17 cells), E-Syt1 KD (n = 33 cells), and E-Syt1/INPP4B DKD (n = 9 cells) cells before and 30 min after nocodazole was added, quantified by cell area still adhering to glass substrate under TIRF imaging. Error bars are in SEM. Specfic p values for paired student's t test are as follows: WT vs E-Syt1 KD: p = 0.003, E-Syt1 vs E-Syt1 / INPP4B DKD: p < 0.0001). Horizontal scale bar for all monographs: 10 μm. Horizontal scale bars for all kymographs: 1 min. Vertical scale bars for all kymographs: 10 μm.

with KD of E-Syt1, which is a major membrane contact site protein in RBL cells and negative regulator of PI(4)P on the plasma membrane through lipid transfer from plasma membrane to endoplasmic reticulum (ER).[57–59] A majority of Rho oscillations in E-Syt1 KD displayed mixed-mode oscillation (18 experiments, 21/37 cells [57%]) (Figures 2C and 2F). Importantly, the mixed-mode oscillation in PTEN or E-Syt1 KD cells has much sharper nested pulses compared to WT cells, which can be captured in wavelet analysis as two separate peaks in the high- and low-frequency regimes (Figures 2E, 2F, and S1).

High-frequency Rho pulses regulated by PIP_3 and $PI(3,4)P_2$

The well-resolved high-frequency pulses in E-Syt1 KD cells provide a dynamical state where the underlying circuit for fast oscillations can be experimentally studied. Because PTEN is a negative regulator of PIP_3, we hypothesize that the high-frequency nested peaks are PIP_3 dependent. PIP_3 could regulate these high-frequency oscillations either by regulating the synthesis or degradation of $PI(3,4)P_2$. We next performed double knockdown (DKD) of E-Syt1 and SHIP1, the enzyme responsible for converting PIP_3 to $PI(3,4)P_2$, or INPP4B, the enzyme that degrades $PI(3,4)P_2$. Mixed-mode oscillations were eliminated in E-Syt1/INPP4B DKD cells but not in E-Syt1/SHIP1 DKD cells (Figure 2C). All the E-Syt1/INPP4B DKD cells imaged displayed simple patterns where high-frequency peaks were reduced or disappeared in the wavelet analysis (4 experiments, 9 cells), indicating INPP4B is responsible for the sharp, nested peaks (Figure 2G). Similarly, lowering PIP_3 had a smoothing effect on the high-frequency nested peaks. When LY294002, an inhibitor of PI3K, was applied to E-Syt1 KD cells displaying nested frequencies, LY294002 caused disappearance of sharp peaks instantly (Figures 2H and 2I). These suggest that the high-frequency peaks are regulated by PIP_3/INPP4B pathway (Figure 2J), where a high level of PIP_3 leads to faster degradation of $PI(3,4)P_2$ and sharper peaks, while a low level of PIP_3 leads to slower degradation of $PI(3,4)P_2$ and merging of multiple high-frequency peaks, which appear as single peaks with long duration.

Correlation between dynamical regimes of Rho oscillations and contractile behavior

To determine whether different modes of Rho oscillations have functional impact on cell contractility, we monitored changes of cell shape using differential interference contrast (DIC) microscopy. WT cells displayed significant changes in cell shape compared to E-Syt1 KD cells (Figures 3A and 3B). These changes in cell shape also correlated with loss of adhesion area monitored by TIRF. WT cells adhered to a smaller area before nocodazole treatment and contracted significantly upon nocodazole treatment, retaining 66.6% ± 6.1% of their cell size (from 676.4 ± 512.0 μm^2 to 426.4 ± 329.2 μm^2, n = 17 cells) (Figure 3C). In comparison, E-Syt1 KD cells did not contract much after the same treatment (from 1,007.0 ± 336.4 μm^2 to 900.3 ± 386.8 μm^2, 88.8% ± 4.1%, n = 33 cells, Figure 3D). These results suggest

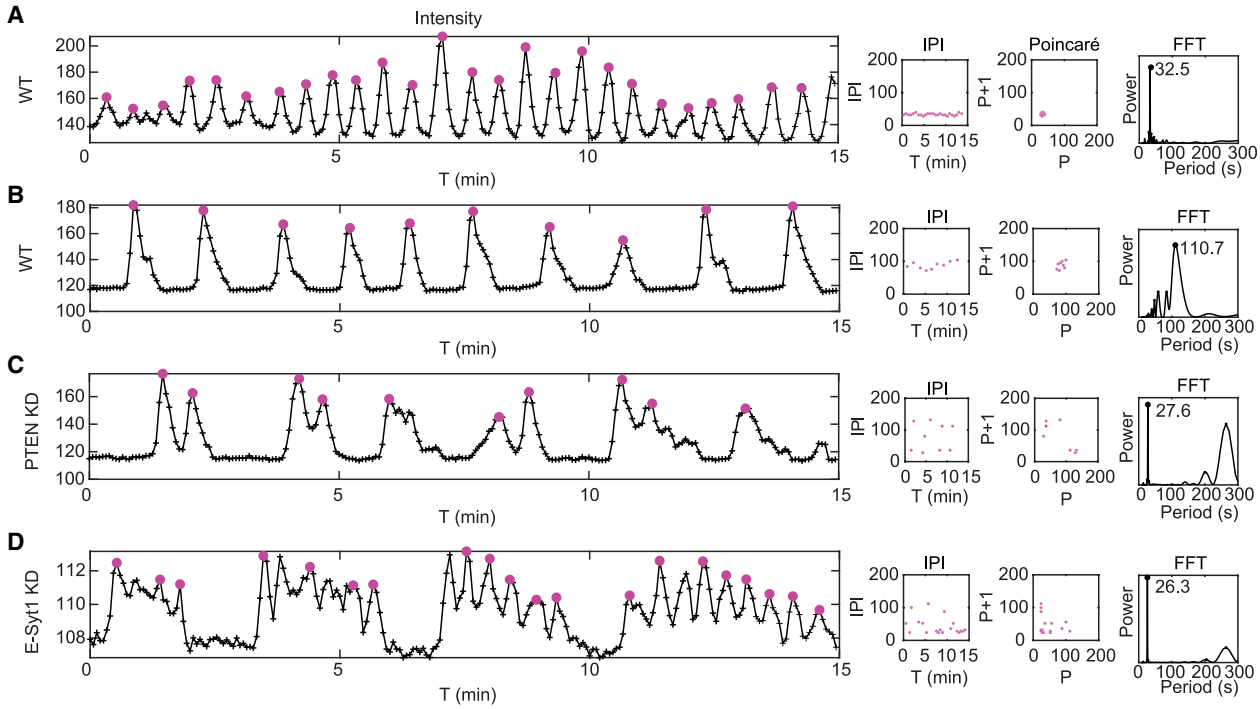

Figure 4. Analysis of line intensity profiles, interpeak intervals (IPIs), Poincaré (P vs. P+1) analysis, and fast Fourier transform (FFT) of representative movies displaying simple and complex oscillations

(A and B) Simple oscillations with different periodicities (56/87 oscillations).

(C) Mixed-mode oscillation with large-amplitude oscillations intercalated by double peaks (3/87 oscillations).

(D) Mixed-mode oscillations that are intercalated by small-amplitude oscillations, with three to four intercalated peaks (28/87 oscillations). Intensity profiles display the selected peaks for IPI and Poincaré analyses. FFT of all plots for both simple and complex Rho oscillations identifies the major peak.

that high-frequency pulses in the mixed-mode oscillations (~30 s) are likely unproductive. E-Syt1 KD cells already adhered to a larger area before nocodazole treatment, and these larger adhesive areas in E-Syt1 KD cells are also potentially consistent with a constitutively reduced level of contractility in these cells. To determine whether converting mixed-mode oscillations in E-Syt1 KD cells back to simple oscillations can rescue contractility, we examined the phenotype of E-Syt1/INPP4B DKD cells. Similar to WT cells, E-Syt1/INPP4B DKD cells contracted significantly as seen by DIC and greatly reduced in footprint sizes upon nocodazole treatment (from 770.7 ± 252.7 μm^2 to 362.1 ± 302.4 μm^2, 45.8% ± 8.9%, n = 9 cells, Figures 3E and 3F). Together, these results suggest a strong correlation between Rho oscillation patterns and the outcome of cell contractility, where persistent Rho signals generate more productive contractility, while short bursts with similar total durations were less effective.

Period-doubling bifurcation with alternating fast and slow cycles

Coupled oscillators can lead to much more complex dynamics including chaos, where the trajectory never repeats itself. The system typically goes through a period-doubling bifurcation and transit from a simple oscillator to a "period two" state, with alternating fast and slow period, which is an intermediate toward chaos. To determine whether a period-doubling bifurcation occurred,[60] we generated a return map (Poincaré plot) by plotting the interpeak interval (P1) relative to the next interpeak interval (P+1). Period-doubling bifurcation can be defined to have taken place if slope of the linear regression in a return map is negative. Simple oscillations are defined as having only a single cluster on the Poincaré plot (56/87 oscillations) (Figures 4A and 4B). Period two states were not common but can be reproducibly found (3 cells out of 87 cells) (Figure 4C). These states consist of large-amplitude oscillations intercalated by double peaks, and the interpeak interval of Rho oscillations falls into two clusters with a negative slope (Figure 4C). The most common form of mixed-mode oscillation consists of large-amplitude oscillations that are intercalated by three to four small-amplitude oscillations (28/87 oscillations). Three clusters can be found on the Poincaré plot (Figure 4D). The duration between the major peak of one oscillatory cycle to the next is approximately 120 s, while the peak-to-peak duration of the small-amplitude oscillations within the major peak's oscillatory cycle is approximately 30 s (Figures 4C and 4D). Again, most rise phases of either mixed-mode oscillations or double peaks are similar, all approximately 20 s. Appearance of these period-doubling events indicates that a second stable oscillatory circuit likely exists.

Substrate depletion mechanism regulates slow Rho oscillation circuit

To understand the slow oscillatory circuit mechanistically, we applied chemical inhibitors to determine whether the period of

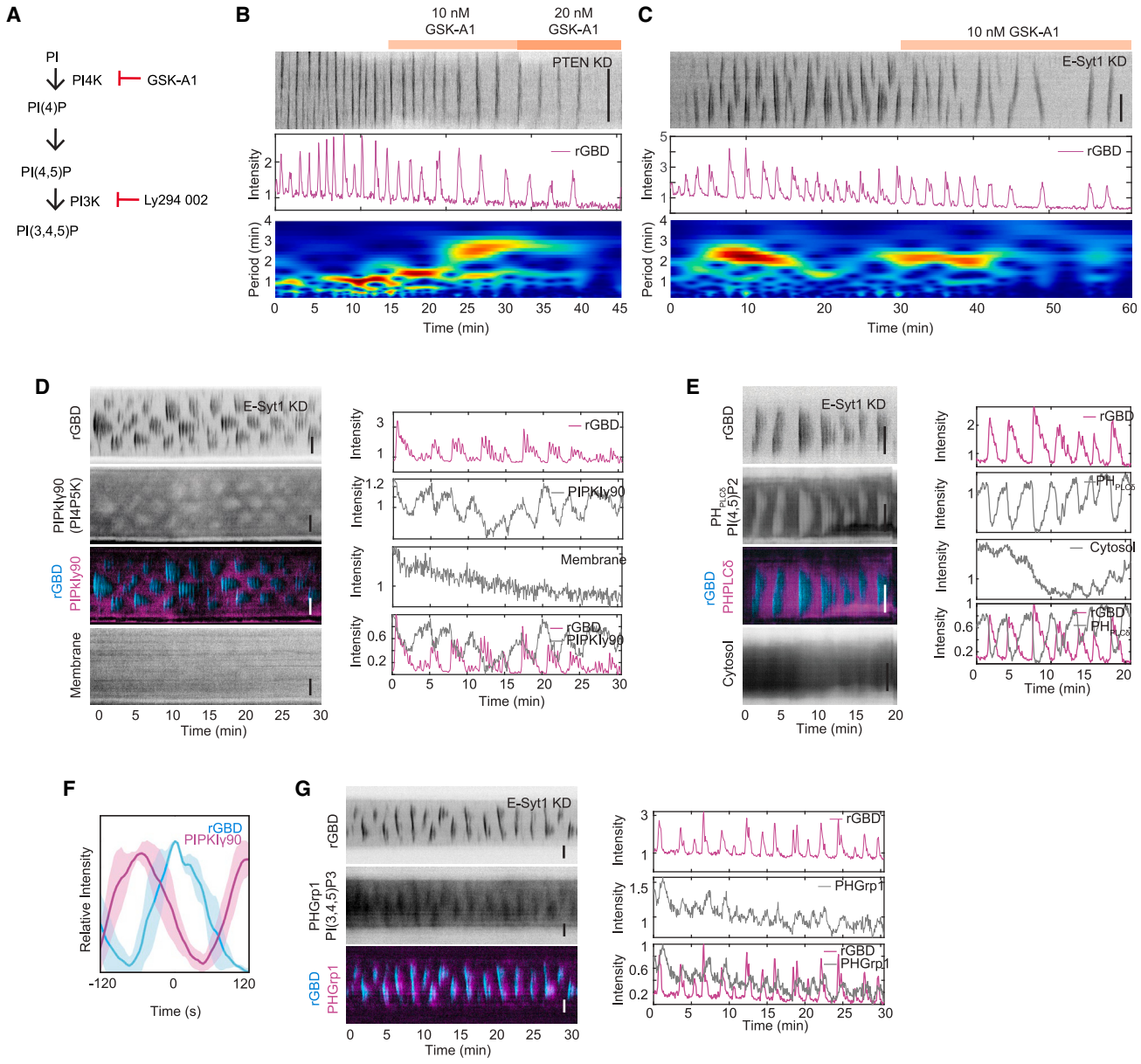

Figure 5. PI4K regulates the frequency of slow Rho oscillations

(A) Schematic depicting the site of action for the inhibitor. LY294002 inhibits PI3K, while GSK-A1 inhibits PI4K.

(B and C) Kymograph, intensity profile, and wavelet analyses of Rho oscillations in PTEN KD and E-Syt1 KD cells upon addition of PI4K inhibitor GSK-A1.

(D) Representative kymograph and intensity profile of Rho in E-Syt1 KD cell co-imaged with PIPKIγ90 (PI4P5K) and the membrane marker iRFP-CAAX (3 experiments, n = 3 cells).

(E) Representative kymograph and intensity profile of Rho in E-Syt1 KD cell co-imaged with $PH_{PLC\delta}$ ($PI(4,5)P_2$) and mCherry as a cytosol marker (3 experiments, n = 3 cells).

(F) Average profiles obtained by aligning peaks of rGBD and PIPKIγ90. The solid lines represent the mean intensities of the profile, and shaded region represents the standard deviations of the intensities.

(G) Representative kymographs and intensity profiles of Rho in E-Syt1 KD cell co-imaged with PH_{Grp1} ($PI(3,4,5)P_3$). Vertical scale bars: 10 μm.

slow cycle can be modulated (Figure 5A). We first examined the effect of LY294002 on slow cycle in cells displaying both complex and simple oscillations. The effect of LY294002 on the slow cycle was not consistent. LY294002 slowed down the major period in simple oscillations (Figures S2A and A′), while it increased the period in complex oscillations in PTEN KD cells (7 experiments, 12 cells) (Figures S2B, B′, C, and C′). These results suggest that the effect of LY294002 on the slow circuit is complex and likely depends on the initial conditions. We next perturbed PI(4)P metabolism by the pharmacological inhibition of PI4K using

PI4Kα-specific inhibitor GSK-A1 (Figure 5A). Inhibition of PI4K reduced the frequencies of simple oscillations (5 experiments, 9/9 cells). In simple oscillations with period of ~60 s, inhibiting PI4K leads to increased oscillation period of ~150 s (Figure 5B). This effect was seen in both WT cells as well as PTEN KD cells. When GSK-A1 was added to cells displaying complex Rho oscillations in E-Syt1 KD cells, mixed-mode oscillation first transited into simple oscillations, followed by a reduction of Rho oscillation periodicity until the oscillations completely stopped (n = 7 experiments, 8/8 cells) (Figure 5C). After GSK-A1 washout, Rho oscillations recovered, indicating the effect was reversible (Figure S3).

The possibility that PI(4)P synthesis could regulate the periodicity of Rho oscillation is surprising because oscillation period is typically regulated by the lifetime of inhibitor in the activator-delayed inhibitor model. PI(4)P could directly recruit Rho, or PI(4)P could serve as a precursor for $PI(4,5)P_2$, which according to any prior knowledge, should be the activator. To better understand how PI4K regulates slow oscillation cycles, we imaged PI4P5K, which converts PI(4)P into $PI(4,5)P_2$. Interestingly, PI4P5K as monitored by PIPKIγ90 levels was depleted when Rho was activated (Figure 5D). This depletion was not caused by the loss of TIRF signal due to membrane fluctuations as the same depletion was not seen by a CAAX membrane marker concurrently imaged in the same cell (3 experiments, n = 3 cells) (Figure 5D). Consistent with the depletion of PI4P5K in sync with Rho activation, an anti-coupling was observed for $PI(4,5)P_2$ and Rho (Figure 5E), suggesting that the level of $PI(4,5)P_2$ was also depleted when Rho activity was elevated. Rho-induced contractility could induce membrane bending and loss of TIRF signals, but here the loss of TIRF signal resulting from membrane fluctuations was much less compared to the reduction of $PI(4,5)P_2$ (Figure 5E), indicating the depletion was real (3 experiments, n = 3 cells). The apparent anti-correlation between Rho and $PI(4,5)P_2$ or PI4P5K may seem to be counter-intuitive given the known positive association between PI4P5K and Rho, but by analyzing their temporal profile with higher time resolution, it is clear that there was still significant overlap between PI4P5K and Rho in time (Figure 5F). In particular, the rise of Rho occurred when PI4P5K level was high (Figure 5F). To determine whether PIP_2 was required for Rho recruitment, we co-transfected the Rho sensor (mCherry-rGBD) with a membrane anchor trap (CIBN-pmGFP) and a CRY2-tagged 5-phosphatase domain of INPP5E (iRFP-CRY2-5-ptase$_{INPP5E}$), whose preferred substrate is $PI(4,5)P_2$. Upon blue-light exposure, iRFP-CRY2-5-ptase$_{INPP5E}$ was recruited to CIBN and rapidly degraded PIP_2 levels in resting cells (n = 3 cells) as well as Rho levels (Figure S4), suggesting that $PI(4,5)P_2$ was still required for Rho recruitment. Thus, the apparent $PI(4,5)P_2$ depletion was the result of a dynamic flux, where the production of $PI(4,5)P_2$ was less than its consumption, but $PI(4,5)P_2$ was continuously generated. To test whether $PI(4,5)P_2$ was converted to PIP_3, we co-imaged PH_{Grp1}, a sensor that binds to PIP_3, with Rho sensor and found that PIP_3 was elevated relative to basal level (Figure 5G). Collectively, this suggests that during the slow cycle of Rho oscillation, $PI(4,5)P_2$ is depleted as a result of a net efflux, and the replenishment rate of $PI(4,5)P_2$ from PI(4)P regulates the oscillation period.

Modulating actomyosin does not switch dynamical regimes of Rho signaling

To examine whether components of the actomyosin cytoskeleton could also share the ability of phosphoinositide metabolism pathways to promote or reduce mixed-mode Rho oscillations, we examined the dynamics of cytoskeletal components. Formins are a group of proteins that are involved in Rho-dependent actin polymerization. We found that mDia3 can also oscillate in the metaphase cells treated with nocodazole (Figure 6A). When mDia3 was co-imaged with rGBD, their oscillations were in phase (Figure 6B). To inhibit actin polymerization mediated by formin, we used inhibitor SMIFH2. The addition of SMIFH2 stopped rGBD oscillations in an all or none fashion (Figure 6C). Myosin IIA also oscillated with rGBD with a phase lag of 12 s (Figures 6D and 6E). Myosin inhibitor blebbistatin stopped rGBD oscillations without an intermediate effect (Figures 6F and 6G). Finally, we added Y-27632 to inhibit ROCK, which is a downstream effector of RhoA. Y-27632 inhibits ROCK by competing with ATP for binding to ROCK's catalytic site. The action of Y-27632 was slower than SMIFH2 and blebbistatin, and an intermediate effect could be found. Interestingly, rGBD oscillations reduced amplitude gradually until they stopped (Figures 6H and 6I). Together, these data suggest that the fine-tuning of simple to mixed-mode oscillations and vice versa is more readily achieved by manipulating phosphoinositide metabolism. While these data do not exclude the possibility that modulating actomyosin could fine-tune Rho signaling, they do not argue strongly that these downstream events exert critical control over the bifurcation point between simple and complex oscillatory regimes.

DISCUSSION

Circuits generated by antagonistic reactions have gained increasing recognition for their role in the organization of signaling events, and these paradoxical regulatory loops frequently lead to oscillations. In this paper, we unveil two such circuits that govern the spatiotemporal dynamics of lipid metabolism and their impact on Rho oscillations. The first major progress we made is realizing that the heterogeneity of Rho dynamics cannot be solely attributed to a single negative regulator. Mixing data with simple and complex oscillation initially led us to wonder whether inhibiting PI3K leads to both increase and decrease of oscillation frequency, and this path turned out to be futile. While complex oscillatory phenomena resulting from the coupling of two oscillators have been extensively studied *in vitro* within chemical and enzymatic reactions, they have not been widely recognized in living cells. One possible reason is that unlike chemical or biochemical reaction conducted in test tubes, where robust oscillations can be readily achieved, so deviation from perfect oscillations can be easily recognized, oscillations in living cells by default appear to be noisy. The inherent noise observed in oscillations of living cells makes it challenging to differentiate between a time series regulated by a simple feedback loop and deterministic complex dynamics governed by interconnected networks. Furthermore, as we have shown here, the dynamic behavior of oscillations in living cells could be sensitive to slight parameter changes. Thus, genetically identical cells can exist in different dynamical states for signaling. This presents additional complexities for

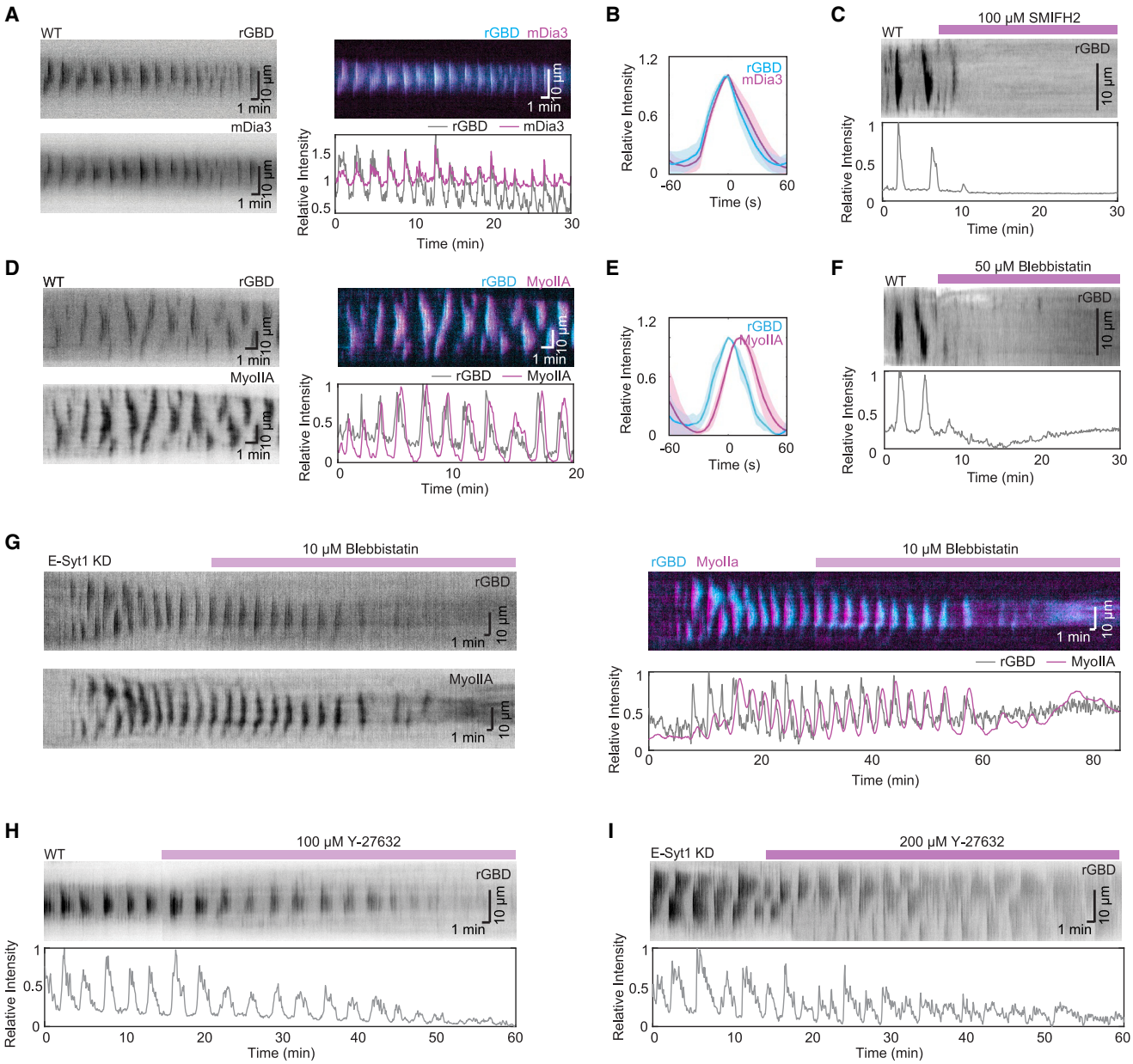

Figure 6. Modulating actomyosin does not switch dynamical regimes of Rho signaling

(A) Kymographs and intensity profile of rGBD (gray) and mDia3 (magenta) oscillations.

(B) Average profiles by aligning peaks of rGBD (cyan) and mDia3 (magenta). The solid lines represent the mean intensities of the profile, and shaded region represents the standard deviations of the intensities.

(C) Kymograph and intensity profile of rGBD oscillations before and after the addition of formin inhibitor SMIFH2.

(D) Kymograph and intensity profile of rGBD (gray) and myosin IIA (magenta) oscillations.

(E) Average profiles of rGBD (cyan) and myosin IIA (magenta).

(F) Kymograph and intensity profile of rGBD oscillations before and after the addition of 50 μM myosin inhibitor blebbistatin.

(G) Kymograph and intensity profile of rGBD (gray) and myosin IIA (magenta) oscillations before and after the addition of 10 μM myosin inhibitor blebbistatin.

(H and I) Kymographs and intensity profiles of rGBD oscillations in wild-type and E-Syt1 KD cells prior to and following addition of ROCK inhibitor Y-27632. Horizontal scale bars: 1 min. Vertical scale bars: 10 μm.

single-cell studies and further complicates our understanding of these systems.

Upon realizing the importance of distinguishing between simple and complex oscillations, our next task was to uncover the conditions that drive transitions between these two regimes of oscillatory behaviors. We successfully identified two such conditions in our study. Firstly, we demonstrated that KD of PTEN leads to an increase in complex mixed-mode oscillations of

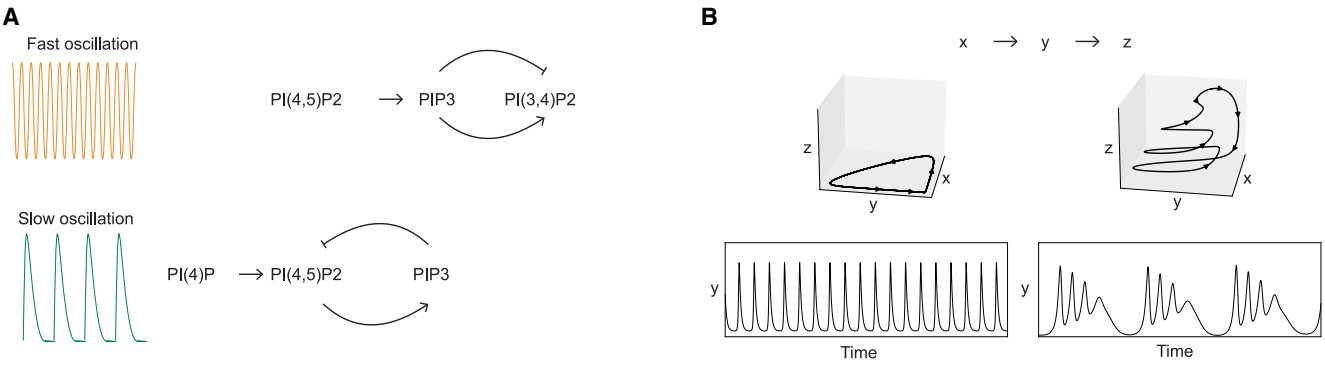

Figure 7. The dynamics of the phosphoinositide network that regulates Rho activation display qualitative similarity to the food chain model developed in ecology that describes chaotic prey-predator relationships

(A) Topological representation of phosphoinositide metabolism that regulates fast and slow Rho oscillations.

(B) Simple and mixed-mode oscillations can be recapitulated using Hastings and Powell model. Trajectories are plotted with parameters values set as $a_1 = 7$ (simple oscillations), $a_1 = 5$ (mixed-mode oscillations), $b_1 = 3$, $a_2 = 0.1$, $b_2 = 2$, $d_1 = 0.4$, and $d_2 = 0.01$.

Rho. This effect is partially attributed to elevated PIP_3 levels, as inhibiting PI3K in PTEN KD cells resulted in a reduction of complex oscillations. Secondly, we discovered that KD of E-Syt1, a protein responsible for tethering the ER to the plasma membrane and facilitating lipid transfer from the plasma membrane to the ER, enhances mixed-mode oscillatory behaviors in a larger number of cells compared to PTEN KD. Interestingly, while PI(4)P, $PI(4,5)P_2$, and PIP_3 are interconnected metabolically, KD of Synaptojanin 2, which should increase $PI(4,5)P_2$ levels, did not produce similar effects. This highlights the presence of nonlinear effects within the network, and it is not a specific lipid or enzyme per se that regulates the network output but its connectivity.

Two commonly employed topologies of oscillations are the activator-inhibitor scheme and the activator-depleted substrate scheme.[61] In the activator-inhibitor model, oscillation occurs when the inhibitory component acts with a delay that prevents immediate cancellation of the activation signal. On the other hand, in the activator-depleted substrate model, oscillations arise when the production rate of substrate could not maintain the production rate of the activator. Our analysis is consistent with the activator-inhibitor model for the fast circuit, while the activator-depleted substrate model is involved in setting the slow circuit (Figure 7A). In WT cells, the fast circuit is hard to resolve. Using PTEN KD- or E-Syt1 KD-induced mixed-mode oscillation, we were able to observe fast oscillations occurring at approximately 30 s, which correlated with high levels of PIP_3. Furthermore, the fast pulses disappeared upon KD of INPP4B, an enzyme responsible for degrading $PI(3,4)P_2$. These findings suggest the presence of an incoherent feedforward loop (PIP_3 -> $PI(3,4)P_2$; PIP_3 -> INPP4 –| $PI(3,4)P_2$) where PIP_3 both serves as a precursor for $PI(3,4)P_2$ and activates its turnover. Regarding the slow circuit, which oscillates at approximately 1–2 min, we observed depletion of $PI(4,5)P_2$, and reducing PI4K activity resulted in a longer oscillation period. These observations support an activator-depleted substrate scheme in which the synthesis of $PI(4,5)P_2$ from PI(4)P occurs at a slower rate compared to the conversion of $PI(4,5)P_2$ to PIP_3, leading to its depletion. The rate of replenishment of PI(4)P then regulates the speed of the cycle. Combining the activator-inhibitor model with the activator-depleted substrate model can serve as a logical design principle for constructing hierarchical networks exhibiting complex dynamics. In the activator-inhibitor model, the duration of the inhibitor's presence determines a refractory period following the activator's phase. Conversely, in the activator-depleted substrate model, the phase during which the substrate is replenished does not impose refractoriness for activation, allowing for sub-cycles of activation within a given slow cycle to occur.

Our main findings highlight the significant role of the phosphoinositide network in regulating Rho dynamics, through its potential for organizing tandem or parallel feedback loops operating at fast and slow timescales. Because Rho oscillations were triggered by nocodazole, which depolymerizes microtubules, our work also suggests that metaphase cortex is poised at the edge of chaos, and microtubules may play a crucial role in regulating the state transition from simple to complex oscillation or between different dynamical states, potentially by modulating phosphoinositide signaling. The involvement of microtubules in cell division has been extensively studied over many decades; however, it remains a complex question, as microtubules serve multiple roles, both positive and negative, depending on the timing and location within the cell.[62–64] From a conceptual standpoint, activating an activator is equivalent to inhibiting an inhibitor. Therefore, relying solely on endpoint measurements would not provide sufficient information to unravel the functional circuitry. Understanding the underlying network governing Rho activation in the mixed-mode oscillation regime will provide a framework to further dissect the multifaceted involvement of microtubules.

Coupled excitable networks have emerged as a fundamental organizing principle for the regulation of chemotaxis.[65] However, coupled oscillatory networks exhibit distinct dynamical states compared to coupled excitable networks. To precisely characterize these differences, a geometric definition of dynamical states is essential.[66,67] In the framework of dynamical systems, an excitable state refers to a specific state characterized by a "fixed-point attractor" in phase space.[68] In this state, fixed points are stable, indicating that the system returns to the

same point in phase space after a perturbation. Trajectories in the excitable regime are relatively close to equilibrium. In a coupled excitable network, the slow circuit could modulate the excitability of the fast network, while the system remains in the regime of "fixed-point attractor."[69] In contrast, oscillations are characterized by a "limit-cycle attractor," representing an alternative steady state where the fixed points become unstable, and trajectories in phase space converge into closed loops. The transition from an excitable state to a limit-cycle state is commonly referred to as a Hopf bifurcation. However, the transition described in this work, from simple to complex oscillations, corresponds to a different bifurcation known as a period-doubling bifurcation.[70] This bifurcation leads the system from a "limit-cycle attractor" to a "period two" state and can ultimately result in chaos, represented by a "strange attractor" where the trajectory never repeats itself. Complex oscillations, such as mixed-mode oscillations and chaos, are further away from equilibrium and cannot be accurately described within a two-dimensional phase plane analysis typically employed to describe excitability, as the trajectories would intersect.

A natural question that arises is whether these higher dimensional attractor states hold physiological relevance. If we assume that physiological significance is determined by the amount of time a cell spends in these states, the excitable or fixed-point attractor state is likely the most physiologically relevant. In most systems, Rho pulses are infrequent and highly irregular. Although not rigorously tested, the experimental data likely correspond to the fixed-point attractor state, which is fundamental for cell homeostasis. The limit-cycle attractor state may be the physiological state for specialized systems such as muscle contraction, similar to the electric activity in the brain or the heart. Higher dimensional attractor states, like the one described in our work, would not be necessary if the sole purpose of the system was to return to the same steady state. However, these dynamical architectures would be advantageous if the system requires the ability to sample different states or settle into new steady states.

The tendency to generate complex oscillations is likely widespread since coupling two circuits with a minimum of three chemical species is sufficient to generate these complex dynamics. The observed dynamics of the phosphoinositide network regulating Rho activation exhibit qualitative similarities to the food chain model developed in ecology, which describes chaotic prey-predator relationships.[71] In this three-species food chain model, coupling a fast cycle between X (prey) and Y (predator) with a slow cycle between Y (predator) and Z (super-predator) leads to various state transitions from fixed points to limit cycles, as well as period doubling or mixed-mode oscillations (Figures 7B and S5). Thus, it seems that how chaos is suppressed under physiological conditions is an equally valid question. Therefore, the focus should not solely be on whether the presence of complex oscillations or chaotic states is actively suppressed or if systems can exist "far enough" from equilibrium to enable the sampling of different attractor states as a distinct feature. With better understanding of the bifurcation points and the ability to control state transitions that occur in these systems, one could then address the implications of these transient but likely crucial events. Importantly, understanding biological systems through attractor dynamics and state transitions will have broad applicability in the study of signal transduction networks and various network-related phenomena in diverse cellular contexts.

Limitations of the study

A fundamental question persists regarding how we experimentally define the distance from equilibrium.[44] While there is a general acceptance that biological systems operate "far" from equilibrium, how far is far? Mechanistic dissection of these functional circuits also remains limited. In particular, the analysis of the elementary reactions involved here has not been completed. It is yet to be established how the same metabolic network of PI(4)P - > PI(4,5)P_2 -> PIP_3 -> PI(3,4)P_2 supports two circuits operating at different timescales, potentially involving different PI4K IIIα complexes[72] and control of lipid fluxes. We expect both circuits involve PIP_3, but the existence of a parallel pathway involving PI(4)P - > PI(3,4)P_2, bypassing PIP_3, could not be ruled out. Finally, we have only visualized PI(4,5)P_2 and PIP_3 using fluorescent lipid sensors in the current work. Direct visualization of PI(4)P and PI(3,4)P_2 would be desirable. Future work is needed to determine whether expression levels of the lipid sensors potentially affect systems dynamics since these lipids serve as critical control parameters themselves.

STAR★METHODS

Detailed methods are provided in the online version of this paper and include the following:

- KEY RESOURCES TABLE
- RESOURCE AVAILABILITY
  - Lead contact
  - Materials availability
  - Data and code availability
- EXPERIMENTAL MODEL AND STUDY PARTICIPANT DETAILS
  - RBL-2H3 cells
- METHOD DETAILS
  - Materials
  - Transfection and knock down
  - Imaging
  - Numerical methods
- QUANTIFICATION AND STATISTICAL ANALYSIS
  - Quantification and image analysis
  - Statistical analysis

SUPPLEMENTAL INFORMATION

Supplemental information can be found online at https://doi.org/10.1016/j.celrep.2023.112857.

ACKNOWLEDGMENTS

We thank members of the Wu lab for discussion and Pietro De Camilli, Jian Liu, and Martin Schwartz for feedback on the manuscript. This work was supported by a Yale University startup grant (M.W.).

AUTHOR CONTRIBUTIONS

Conceptualization, M.W. and C.S.T.; methodology, M.W., C.S.T., and X.J.X.; software, M.W. and X.J.X.; validation, C.S.T.; formal analysis, C.S.T.; writing – original draft, M.W. and C.S.T.; writing – review & editing, M.W. and C.S.T.;

visualization, C.S.T.; supervision, M.W.; project administration, M.W.; funding acquisition, M.W.

DECLARATION OF INTERESTS

The authors declare no competing interests.

INCLUSION AND DIVERSITY

We support inclusive, diverse, and equitable conduct of research.

DECLARATION OF GENERATIVE AI AND AI-ASSISTED TECHNOLOGIES IN WRITING PROCESS

ChatGPT (https://chat.openai.com) was used to check grammar. The authors take full responsibility for the content of the publication.

Received: December 9, 2022
Revised: June 1, 2023
Accepted: July 7, 2023
Published: July 25, 2023

REFERENCES

1. Basant, A., and Glotzer, M. (2018). Spatiotemporal Regulation of RhoA during Cytokinesis. Curr. Biol. *28*, R570–R580. https://doi.org/10.1016/j.cub.2018.03.045.
2. Michaud, A., Leda, M., Swider, Z.T., Kim, S., He, J., Landino, J., Valley, J.R., Huisken, J., Goryachev, A.B., Von Dassow, G., and Bement, W.M. (2022). A versatile cortical pattern-forming circuit based on Rho, F-actin, Ect2, and RGA-3/4. J. Cell Biol. *221*, e202203017–e202203021. https://doi.org/10.1083/jcb.202203017.
3. Swider, Z.T., Michaud, A., Leda, M., Landino, J., Goryachev, A.B., and Bement, W.M. (2022). Cell cycle and developmental control of cortical excitability in Xenopus laevis. Mol. Biol. Cell *33*, ar73–13. https://doi.org/10.1091/mbc.E22-01-0025.
4. Bement, W.M., Leda, M., Moe, A.M., Kita, A.M., Larson, M.E., Golding, A.E., Pfeuti, C., Su, K.C., Miller, A.L., Goryachev, A.B., and von Dassow, G. (2015). Activator-inhibitor coupling between Rho signalling and actin assembly makes the cell cortex an excitable medium. Nat. Cell Biol. *17*, 1471–1483. https://doi.org/10.1038/ncb3251.
5. Tan, T.H., Liu, J., Miller, P.W., Tekant, M., Dunkel, J., and Fakhri, N. (2020). Topological turbulence in the membrane of a living cell. Nat. Phys. *16*, 657–662. https://doi.org/10.1038/s41567-020-0841-9.
6. Yao, B., Donoughe, S., Michaux, J., and Munro, E. (2022). Modulating RhoA effectors induces transitions to oscillatory and more wavelike RhoA dynamics in Caenorhabditis elegans zygotes. Mol. Biol. Cell *33*, ar58-16. https://doi.org/10.1091/mbc.E21-11-0542.
7. Bell, K.R., Werner, M.E., Doshi, A., Cortes, D.B., Sattler, A., Vuong-Brender, T., Labouesse, M., and Maddox, A.S. (2020). Novel cytokinetic ring components drive negative feedback in cortical contractility. Mol. Biol. Cell *31*, 1623–1636. https://doi.org/10.1091/mbc.E20-05-0304.
8. Nishikawa, M., Naganathan, S.R., Jü Licher, F., and Grill, S.W. (2017). Controlling contractile instabilities in the actomyosin cortex. Elife *6*, 1–21. https://doi.org/10.7554/eLife.19595.001.
9. Gerisch, G., Prassler, J., and Ecke, M. (2022). Patterning of the cell cortex and the localization of cleavage furrows in multi-nucleate cells. J. Cell Sci. *135*, jcs259648–11. https://doi.org/10.1242/jcs.259648.
10. Xiao, S., Tong, C., Yang, Y., and Wu, M. (2017). Mitotic Cortical Waves Predict Future Division Sites by Encoding Positional and Size Information. Dev. Cell *43*, 493–506.e3. https://doi.org/10.1016/j.devcel.2017.10.023.
11. Murthy, K., and Wadsworth, P. (2008). Dual role for microtubules in regulating cortical contractility during cytokinesis. J. Cell Sci. *121*, 2350–2359. https://doi.org/10.1242/jcs.027052.
12. Zhou, M., and Wang, Y.-L. (2008). Distinct Pathways for the Early Recruitment of Myosin II and Actin to the Cytokinetic Furrow. Mol. Biol. Cell *19*, 318–326. https://doi.org/10.1091/mbc.E07-08.
13. Savoian, M.S., Khodjakov, A., and Rieder, C.L. (1999). Unilateral and wandering furrows during mitosis in vertebrates: Implications for the mechanism of cytokinesis. Cell Biol. Int. *23*, 805–812. https://doi.org/10.1006/cbir.1999.0477.
14. Oster, G.F., and Odell, G.M. (1984). Mechanics of Cytogels I: Oscillations in Physarum. Cell Motil. *4*, 469–503.
15. Nagai, R., Yoshimoto, R.N., and Kamiya, N. (1978). Cyclic production of tension force in the plasmodial strand of Physarum polycephalum and its relation to microfilament morphology. J. Cell Sci. *33*, 205–225.
16. Baird, M.A., Billington, N., Wang, A., Adelstein, R.S., Sellers, J.R., Fischer, R.S., and Waterman, C.M. (2017). Local pulsatile contractions are an intrinsic property of the myosin 2A motor in the cortical cytoskeleton of adherent cells. Mol. Biol. Cell *28*, 240–251. https://doi.org/10.1091/mbc.E16-05-0335.
17. Munjal, A., Philippe, J.M., Munro, E., and Lecuit, T. (2015). A self-organized biomechanical network drives shape changes during tissue morphogenesis. Nature *524*, 351–355. https://doi.org/10.1038/nature14603.
18. Graessl, M., Koch, J., Calderon, A., Kamps, D., Banerjee, S., Mazel, T., Schulze, N., Jungkurth, J.K., Patwardhan, R., Solouk, D., et al. (2017). An excitable Rho GTPase signaling network generates dynamic subcellular contraction patterns. J. Cell Biol. *216*, 4271–4285. https://doi.org/10.1083/jcb.201706052.
19. Reinhard, N.R., Van Helden, S.F., Anthony, E.C., Yin, T., Wu, Y.I., Goedhart, J., Gadella, T.W.J., and Hordijk, P.L. (2016). Spatiotemporal analysis of RhoA/B/C activation in primary human endothelial cells. Sci. Rep. *6*, 25502–25516. https://doi.org/10.1038/srep25502.
20. He, L., Wang, X., Tang, H.L., and Montell, D.J. (2010). Tissue elongation requires oscillating contractions of a basal actomyosin network. Nat. Cell Biol. *12*, 1133–1142. https://doi.org/10.1038/ncb2124.
21. Higgins, J. (1967). The Theory of Oscillating Reactions - Kinetics Symposium. Ind. Eng. Chem. *59*, 18–62.
22. Degn, H. (1972). Oscillating Chemical Reactions in Homogeneous Phase. J. Chem. Educ. *49*, 302–307.
23. Avsievich, T.I., Frolov, S.V., and Proskurin, S.G. (2017). Interrelation between respiratory and contractile activity of Physarum polycephalum. J. Phys. D Appl. Phys. *50*, 224003–224007. https://doi.org/10.1088/1361-6463/aa6ce5.
24. Cash, J.N., Sharma, P.V., and Tesmer, J.J.G. (2019). Structural and biochemical characterization of the pleckstrin homology domain of the RhoGEF P-Rex2 and its regulation by PIP3. J. Struct. Biol. X *1*, 100001–100008. https://doi.org/10.1016/j.yjsbx.2018.100001.
25. Lekomtsev, S., Su, K.C., Pye, V.E., Blight, K., Sundaramoorthy, S., Takaki, T., Collinson, L.M., Cherepanov, P., Divecha, N., and Petronczki, M. (2012). Centralspindlin links the mitotic spindle to the plasma membrane during cytokinesis. Nature *492*, 276–279. https://doi.org/10.1038/nature11773.
26. Su, K.C., Takaki, T., and Petronczki, M. (2011). Targeting of the RhoGEF Ect2 to the Equatorial Membrane Controls Cleavage Furrow Formation during Cytokinesis. Dev. Cell *21*, 1104–1115. https://doi.org/10.1016/j.devcel.2011.11.003.
27. Yoshida, S., Bartolini, S., and Pellman, D. (2009). Mechanisms for concentrating Rho1 during cytokinesis. Genes Dev. *23*, 810–823. https://doi.org/10.1101/gad.1785209.
28. Matsuoka, S., and Ueda, M. (2018). Mutual inhibition between PTEN and PIP3 generates bistability for polarity in motile cells. Nat. Commun. *9*, 4481–4515. https://doi.org/10.1038/s41467-018-06856-0.
29. Li, X., Edwards, M., Swaney, K.F., Singh, N., Bhattacharya, S., Borleis, J., Long, Y., Iglesias, P.A., Chen, J., and Devreotes, P.N. (2018). Mutually inhibitory Ras-PI(3,4)P2 feedback loops mediate cell migration. Proc.

Natl. Acad. Sci. USA *115*, E9125–E9134. https://doi.org/10.1073/pnas.1809039115.

30. Masters, T.A., Sheetz, M.P., and Gauthier, N.C. (2016). F-actin waves, actin cortex disassembly and focal exocytosis driven by actin-phosphoinositide positive feedback. Cytoskeleton *73*, 180–196. https://doi.org/10.1002/cm.21287.
31. Xiong, D., Xiao, S., Guo, S., Lin, Q., Nakatsu, F., and Wu, M. (2016). Frequency and amplitude control of cortical oscillations by phosphoinositide waves. Nat. Chem. Biol. *12*, 159–166. https://doi.org/10.1038/nchembio.2000.
32. Taniguchi, D., Ishihara, S., Oonuki, T., Honda-Kitahara, M., Kaneko, K., and Sawai, S. (2013). Phase geometries of two-dimensional excitable waves govern self-organized morphodynamics of amoeboid cells. Proc. Natl. Acad. Sci. USA *110*, 5016–5021. https://doi.org/10.1073/pnas.1218025110.
33. Shibata, T., Nishikawa, M., Matsuoka, S., and Ueda, M. (2012). Modeling the self-organized phosphatidylinositol lipid signaling system in chemotactic cells using quantitative image analysis. J. Cell Sci. *125*, 5138–5150. https://doi.org/10.1242/jcs.108373.
34. Gerisch, G., Schroth-Diez, B., Müller-Taubenberger, A., and Ecke, M. (2012). PIP3 waves and PTEN dynamics in the emergence of cell polarity. Biophys. J. *103*, 1170–1178. https://doi.org/10.1016/j.bpj.2012.08.004.
35. Gerisch, G., Ecke, M., Wischnewski, D., and Schroth-Diez, B. (2011). Different modes of state transitions determine pattern in the Phosphatidylinositide-Actin system. BMC Cell Biol. *12*, 42–15. https://doi.org/10.1186/1471-2121-12-42.
36. Arai, Y., Shibata, T., Matsuoka, S., Sato, M.J., Yanagida, T., and Ueda, M. (2010). Self-organization of the phosphatidylinositol lipids signaling system for random cell migration. Proc. Natl. Acad. Sci. USA *107*, 12399–12404. https://doi.org/10.1073/pnas.0908278107.
37. Posor, Y., Jang, W., and Haucke, V. (2022). Phosphoinositides as membrane organizers. Nat. Rev. Mol. Cell Biol. *23*, 797–816. https://doi.org/10.1038/s41580-022-00490-x.
38. Balla, T. (2013). Phosphoinositides: Tiny Lipids With Giant Impact on Cell Regulation. Physiol. Rev. *93*, 1019–1137. https://doi.org/10.1152/physrev.00028.2012.-Phosphoinositides.
39. Decroly, O., and Goldbeter, A. (1982). Birhythmicity, chaos, and other patterns of temporal self-organization in a multiply regulated biochemical system. Proc. Natl. Acad. Sci. USA *79*, 6917–6921.
40. Tyson, J.J. (1973). Some further studies of nonlinear oscillations in chemical systems. J. Chem. Phys. *58*, 3919–3930. https://doi.org/10.1063/1.1679748.
41. Li, Y., and Goldbeter, A. (1989). Oscillatory Isozymes as the Simplest Model for Coupled Biochemical Oscillators. J. Theor. Biol. *138*, 149–174.
42. Sagués, F., and Epstein, I.R. (2003). Nonlinear chemical dynamics. Dalton Trans., 1201–1217. https://doi.org/10.1039/b210932h.
43. Goldbeter, A. (2002). Computational approaches to cellular rhythms. Nature *420*, 238–245.
44. Awal, N.M., and Epstein, I.R. (2021). Period-doubling route to mixed-mode chaos. Phys. Rev. E *104*, 024211–024225. https://doi.org/10.1103/PhysRevE.104.024211.
45. Yamaguchi, H.Q., Ode, K.L., and Ueda, H.R. (2021). A design principle for posttranslational chaotic oscillators. iScience *24*, 101946–102016. https://doi.org/10.1016/j.isci.2020.101946.
46. Petrov, V., Gáspár, V., Masere, J., and Showalter, K. (1993). Controlling chaos in the Belousov-Zhabotinsky reaction. Nature *361*, 240–243.
47. Schmitz, R.A., Graziani, K.R., and Hudson, J.L. (1977). Experimental evidence of chaotic states in the Belousov-Zhabotinskii reaction. J. Chem. Phys. *67*, 3040–3044. https://doi.org/10.1063/1.435267.
48. Steinmetz, C.G., Geest, T., and Larter, R. (1993). Universality in the Peroxidase-Oxidase Reaction: Period Doublings, Chaos, Period Three, and Unstable Limit Cycles. J. Phys. Chem. *97*, 5649–5653.
49. Steinmetz, C.G., and Larter, R. (1991). The quasiperiodic route to chaos in a model of the peroxidase-oxidase reaction. J. Chem. Phys. *94*, 1388–1396. https://doi.org/10.1063/1.459996.
50. Heltberg, M.L., Krishna, S., and Jensen, M.H. (2019). On chaotic dynamics in transcription factors and the associated effects in differential gene regulation. Nat. Commun. *10*, 71–10. https://doi.org/10.1038/s41467-018-07932-1.
51. Gelens, L., Huang, K.C., and Ferrell, J.E. (2015). How Does the Xenopus laevis Embryonic Cell Cycle Avoid Spatial Chaos? Cell Rep. *12*, 892–900. https://doi.org/10.1016/j.celrep.2015.06.070.
52. McIsaac, R.S., Huang, K.C., Sengupta, A., and Wingreen, N.S. (2011). Does the potential for chaos constrain the embryonic cell-cycle oscillator? PLoS Comput. Biol. *7*, e1002109–e1002110. https://doi.org/10.1371/journal.pcbi.1002109.
53. Novák, B., and Tyson, J.J. (2008). Design principles of biochemical oscillators. Nat. Rev. Mol. Cell Biol. *9*, 981–991. https://doi.org/10.1038/nrm2530.
54. Hara, K., Tydeman, P., and Kirschner, M. (1980). A cytoplasmic clock with the same period as the division cycle in Xenopus eggs. Proc. Natl. Acad. Sci. USA *77*, 462–466.
55. Zhang, J., Guo, W.H., and Wang, Y.L. (2014). Microtubules stabilize cell polarity by localizing rear signals. Proc. Natl. Acad. Sci. USA *111*, 16383–16388. https://doi.org/10.1073/pnas.1410533111.
56. Larter, R., Steinmetz, C.G., and Aguda, B.D. (1988). Fast-slow variable analysis of the transition to mixed-mode oscillations and chaos in the peroxidase reaction. J. Chem. Phys. *89*, 6506–6514. https://doi.org/10.1063/1.455370.
57. Manford, A.G., Stefan, C.J., Yuan, H.L., MacGurn, J.A., and Emr, S.D. (2012). ER-to-Plasma Membrane Tethering Proteins Regulate Cell Signaling and ER Morphology. Dev. Cell *23*, 1129–1140. https://doi.org/10.1016/j.devcel.2012.11.004.
58. Schauder, C.M., Wu, X., Saheki, Y., Narayanaswamy, P., Torta, F., Wenk, M.R., De Camilli, P., and Reinisch, K.M. (2014). Structure of a lipid-bound extended synaptotagmin indicates a role in lipid transfer. Nature *510*, 552–555. https://doi.org/10.1038/nature13269.
59. Giordano, F., Saheki, Y., Idevall-Hagren, O., Colombo, S.F., Pirruccello, M., Milosevic, I., Gracheva, E.O., Bagriantsev, S.N., Borgese, N., and De Camilli, P. (2013). PI(4,5)P2-Dependent and Ca2+-Regulated ER-PM interactions mediated by the extended synaptotagmins. Cell *153*, 1494–1509. https://doi.org/10.1016/j.cell.2013.05.026.
60. Quail, T., Shrier, A., and Glass, L. (2015). Predicting the onset of period-doubling bifurcations in noisy cardiac systems. Proc. Natl. Acad. Sci. USA *112*, 9358–9363. https://doi.org/10.1073/pnas.1424320112.
61. Gierer, A., and Meinhardt, H. (1972). A Theory of Biological Pattern Formation. Kybernetik *12*, 30–39.
62. von Dassow, G. (2009). Concurrent cues for cytokinetic furrow induction in animal cells. Trends Cell Biol. *19*, 165–173. https://doi.org/10.1016/j.tcb.2009.01.008.
63. Burgess, D.R., and Chang, F. (2005). Site selection for the cleavage furrow at cytokinesis. Trends Cell Biol. *15*, 156–162. https://doi.org/10.1016/j.tcb.2005.01.006.
64. D'Avino, P.P., Savoian, M.S., and Glover, D.M. (2005). Cleavage furrow formation and ingression during animal cytokinesis: A microtubule legacy. J. Cell Sci. *118*, 1549–1558. https://doi.org/10.1242/jcs.02335.
65. Iglesias, P.A., and Devreotes, P.N. (2012). Biased excitable networks: How cells direct motion in response to gradients. Curr. Opin. Cell Biol. *24*, 245–253. https://doi.org/10.1016/j.ceb.2011.11.009.
66. Tyson, J.J., and Novak, B. (2020). A Dynamical Paradigm for Molecular Cell Biology. Trends Cell Biol. *30*, 504–515. https://doi.org/10.1016/j.tcb.2020.04.002.
67. Goldbeter, A. (2018). Dissipative structures in biological systems: Bistability, oscillations, spatial patterns and waves. Philos. Trans. A Math. Phys.

Eng. Sci. *376*, 20170376–20170425. https://doi.org/10.1098/rsta.2017.0376.

68. Prigogine, I. (1978). Time, Structure, and Fluctuations. Science *201*, 777–785.
69. Miao, Y., Bhattacharya, S., Banerjee, T., Abubaker-Sharif, B., Long, Y., Inoue, T., Iglesias, P.A., and Devreotes, P.N. (2019). Wave patterns organize cellular protrusions and control cortical dynamics. Mol. Syst. Biol. *15*, 85855–e8620. https://doi.org/10.15252/msb.20188585.
70. May, R.M. (1976). Simple mathematical models with very complicated dynamics. Nature *261*, 459–467.
71. Hastings, A., and Powell, T. (1991). Chaos In A Three-Species Food Chain. Ecology *72*, 896–903.
72. Batrouni, A.G., Bag, N., Phan, H.T., Baird, B.A., and Baskin, J.M. (2022). A palmitoylation code controls PI4KIIIα complex formation and PI(4,5)P2 homeostasis at the plasma membrane. J. Cell Sci. *135*, jcs259365–17. https://doi.org/10.1242/jcs.259365.
73. Schindelin, J., Arganda-Carreras, I., Frise, E., Kaynig, V., Longair, M., Pietzsch, T., Preibisch, S., Rueden, C., Saalfeld, S., Schmid, B., et al. (2012). Fiji: An open-source platform for biological-image analysis. Nat. Methods *9*, 676–682. https://doi.org/10.1038/nmeth.2019.

STAR★METHODS

KEY RESOURCES TABLE

REAGENT or RESOURCE	SOURCE	IDENTIFIER
Chemicals, peptides, and recombinant proteins		
Nocodazole	Millipore Sigma	M1404
GSK-A1	Millipore Sigma	SML2453
LY 294002	Millipore Sigma	L9908
SMIFH2	Millipore Sigma	S4826
(−)-Blebbistatin	Millipore Sigma	B0560
Y-27632	Stem Cell Technologies	72302
FBS	Millipore Sigma	F4135
MEM	Life Technologies	11095098
Trypsin-EDTA (0.25%)	Life Technologies	25200056
Puromycin	Gibco	A1113803
Experimental models: Cell lines		
RBL-2H3 cell	ATCC	Cat#: CRL-2256; RRID:CVCL_0591
Recombinant DNA		
rGFP-GBD rho sensor	Addgene	Cat# 26732; RRID:Addgene_26732 Wu Lab Plasmid ID: G10
mCherry-MyosinIIA	Addgene	Cat# 55105; RRID:Addgene_55105 Wu Lab Plasmid ID: A201
mCherry-mDia3	Subcloned from GFP-mDia3, gift from Shuh Narumiya	Wu Lab Plasmid ID: A99c
mCherry-PIPKIγ90	Subcloned from GFP-PIPKIγ90, gift from Pietro De Camilli	Wu Lab Plasmid ID: P012
iRFP-$PH_{PLC\delta}$	Gift from Pietro De Camilli	Wu Lab Plasmid ID: M242
mCherry-PH_{Grp1}	Gift from Pietro De Camilli	Wu Lab Plasmid ID: M35
E-Syt1 Rat shRNA in retroviral untagged vector	Origene Technologies	TR710045A CCAAGTTCACTTGAGG TTAGAATGGCTATTR710045B TTCCTTCGGACGCCGCTTGT TGGTGCTGGWu Lab shRNA ID: ESYT01 & ESYT02
PTEN Rat shRNA in retroviral untagged vector	Origene Technologies	TR711414A CTTGACCAATGGCTAA GTGAAGACGACAATR711414B ATAGAGCGTGCGGATAA TGACAAGGAGTAWu Lab shRNA ID: SQN01 & SQN02
Synaptojanin-2 Rat shRNA in retroviral RFP vector	Origene Technologies	FI732825 TGTGCCTCTGCGGCAGCA CCAGGTGAACTFI732826 TTGTGGAGACAGAG CAGGCGATTTACATG Wu Lab shRNA ID: SS01 & SS02
INPP4B Rat shRNA in retroviral untagged vector	Origene Technologies	TR712257CAGTGGTCGGCAC CATAGAAGTCAGCCTCGTR 712257DAGCCACCTTCTC CTAAGGTCAGCACAGAG Wu Lab shRNA ID: SRN03 & SRN04
Software and algorithms		
MMO analysis	Written in-house	https://github.com/min-wu-lab/mmo-analysis https://doi.org/10.5281/zenodo.8083400
Fiji (ImageJ)	NIH	http://fiji.sc/

(*Continued on next page*)

Continued

REAGENT or RESOURCE	SOURCE	IDENTIFIER
Prism 9	Graphpad	N/A
MATLAB	Mathworks	N/A
Python	Python Software Foundation	N/A
Other		
Neon Transfection System 10 μL Kit	Life Technologies	MPK1096
35 mm Dish | No. 1.5 Coverslip | 20 mm Glass Diameter | Uncoated	Mattek Corporation	P35G-1.5-20-C

RESOURCE AVAILABILITY

Lead contact

Further information and requests for resources and reagents should be directed to and will be fulfilled by the lead contact, Min Wu (wu.min@yale.edu).

Materials availability

All unique/stable reagents generated in this study are available from the lead contact without restriction.

Data and code availability

All data reported in this paper will be shared by the lead contact upon request. All original code has been deposited on Github and is publicly available as of the date of publication. DOIs are listed in the key resources table. Any additional information required to re-analyze the data reported in this paper is available from the lead contact upon request.

EXPERIMENTAL MODEL AND STUDY PARTICIPANT DETAILS

RBL-2H3 cells

RBL-2H3 cells (female, ATCC) were cultured in Minimum Essential Medium with Earles Salts (MEM) (Invitrogen 1109580) supplemented with 20% Fetal Bovine Serum (Sigma F4135). Cell culture was performed in either a T25 (Corning 430439) or T75 (Falcon 353136) cell culture flasks with vented caps. The cells were maintained in a humidified 5% CO_2 incubator at 37°C. The maximum number of cell passages for cells used in our experiments was limited to 30.

METHOD DETAILS

Materials

The following reagents were purchased from commercial sources: Nocodazole (M1404), GSK-A1, LY294002 (L9908), SMIFH2 (S4826), (−) Blebbistatin (B0560), and Y-27632 (72302) were obtained from Millipore Sigma. The drug stocks were prepared in DMSO at the following concentrations and stored at −20°C: 6.6 mM Nocodazole, 1 mM GSK-A1, 14.5 mM LY294002, 50 mM Blebbistatin, 50 mM SMIFH2 and 50 mM Y-27632. E-Syt1 shRNA in pRS vector (Cat # TR710045A, CCAAGTTCACTTGAGGTTAGAATGGCTAT and TR710045B, TTCCTTCGGACGCCGCTTGTTGGTGCTGG), PTEN shRNA in pRS vector (Cat # TR711414A CTTGACCAATGGCTAA GTGAAGACGACAA and TR711414B, ATAGAGCGTGCGGATAATGACAAGGAGTA), Synaptojanin 2 shRNA in pRFP-C-RS vector (Cat # FI732825, TGTGCCTCTGCGGCAGCACCAGGTGAACT and FI732826, TTGTGGAGACAGAGCAGGCGATTTACATG) were purchased from Origene. We are grateful for the generous gifts of the following protein contructs: GFP-PIPKIγ90, mCherry-PH_{Grp1} and iRFP-$PH_{PLC\delta}$ from Pietro De Camilli (Yale School of Medicine), GFP-mDia3 from Shuh Narumiya (Kyoto University Faculty of Medicine). To generate mCherry-mDia3, we subcloned mDia3 into mCherry-C1 using SacI and BamHI restriction sites. Similiarly, mCherry-PIPKIγ90 was prepared by subcloning PIPKIγ90 into mCherry-C1 using BglII and EcoRI restriction sites. GFP-rGBD (Cat #26732) and mCherry-MyosinIIA (Cat #55105) were obtained from Addgene.

Transfection and knock down

For transfections, electroporation with the Neon transfection system (Invitrogen MPK5000) using the 10 μL kit (MPK1025) was employed. RBL-2H3 cells were trypsinized using Trypsin-EDTA (0.25%) (Life Technologies 25200056), resuspended in 2 mL of RBL-2H3 cell culture medium and counted with a hemacytometer (Marienfeld 0640010). A total of 1.5 x 10^6 RBL-2H3 cells were pelleted, resuspended with 10 μL of the R buffer provided by the transfection kit, and mixed with 1 μg of each plasmid used for co-transfection. The electroporation parameters were set as follows: 1200 pulse voltage, 20 ms pulse width, and 2 pulse number. Following transfection, cells were seeded on 35 mm glass bottom dishes (MatTek P35G-1.5-20-C) and incubated overnight.

For knockdown experiments targeting E-Syt1, PTEN and INPP4B, 1 μg of each respective shRNA was used for each transfection. After knockdown, cells were cultured for 24 h and then treated with 1 μg/mL puromycin (Gibco A1113803) for an additional 24 h before proceeding with imaging experiments.

Imaging

TIRFM experiments were performed using a Nikon TiE inverted microscope equipped with 3 laser lines (488 nm, 561 nm, 642 nm). The microscope was fitted with an iLas2 motorized TIRF illuminator (Roper Scientific) and with a Prime95b sCMOS camera (Photometrics). Nikon objectives including Apo TIRF 100× (N.A. 1.49 oil) and 60× (N.A. 1.49 oil) were used for image acquisition. Sequential excitation with lasers at 491 nm, 561 nm, or 642 nm was employed for imaging cells in two or three channels. A quad-bandpass filter (Di01-R405/488/561/635, Semrock) and single band filters including 520/35 nm for GFP, 609/54 nm for RFP and mCherry, and 692/40 nm for iRFP (Semrock) were utilized accordingly.

The microscope operation was controlled by Metamorph software (Universal Imaging). Throughout the experiments, imaging was performed at a constant temperature of 37°C using an on-stage incubator system (Live Cell Instrument, Seoul, South Korea). Prior to imaging, the media was replaced with pre-warmed imaging buffer Tyrodes [20 mM HEPES (pH = 7.4), 135 mM NaCl, 5.0 mM KCl, 1.8 mM $CaCl_2$, 1.0 mM $MgCl_2$ and 5.6 mM glucose]. Cells were maintained in imaging buffer at 37°C during the entire imaging process. The DIC channel was initially used to identify cells in pro-meta/metaphase. Subsequently, the fluorescent channels were employed to confirm successful transfection and expression of fluorescently tagged proteins. Cells with low expression of Rho sensor rGBD (raw intensity values of 120–150 in our setting) were chosen for imaging to avoid overexpression induced artifacts (we have noticed empirically bright cells do not reliably show Rho oscillations). To induce Rho oscillations, 500 nM Nocodazole was added by diluting it from a stock solution with pre-warmed imaging buffer and added when imaging the pro-meta/metaphase cells. For inhibitor experiments, GSK-A1, LY294002, Blebbistatin, Y-27632 and SMIFH2 were further diluted from frozen stocks with pre-warmed imaging buffer to 2x final concentration. The inhibitors were added during imaging to achieve the desired final concentrations. All image sequences were acquired at a time interval of 4 s.

Numerical methods

Simple and mixed-mode Rho oscillations are recapitulated using the Hastings and Powell model, originally developed in ecology to describe chaotic prey-predator relationships.[71] The system of equations governing the model shown in Figure 7 takes the form of

$$\dot{x} = x(1-x) - \frac{a_1 x}{1+b_1 x} y$$

$$\dot{y} = \frac{a_1 x}{1+b_1 x} y - \frac{a_2 y}{1+b_2 y} z - d_1 y$$

$$\dot{z} = \frac{a_2 y}{1+b_2 y} z - d_2 z$$

where $x,y,z \geq 0$. Numerical integration of these stiff first order ordinary differential equations is performed using Python (Anaconda, Inc), including the SciPy and NumPy libraries. The system is integrated with a time step of $\Delta t = 0.05$ for 10^5 steps, which is sufficient for convergence. Parameters are set to be $a_1 = 5$, $b_1 = 3$, $a_2 = 0.1$, $b_2 = 2$, $d_1 = 0.4$, $d_2 = 0.01$ for mixed-mode oscillations. Initial conditions in Figure 7B are (1,1,10). Within the domain of initial conditions used, the differences in initial conditions only influence the rate of convergence to the attractor state, but not the attractor state itself.

QUANTIFICATION AND STATISTICAL ANALYSIS

Quantification and image analysis

The acquired images were in 16-bit format and had dimensions of 1200 x 1200 pixels. The pixel size was 0; 183 μm/pixel when imaged with a 60× objective and 0; 11 μm/pixel when imaged with a 100× objective. For the generation of displayed kymographs, Fiji software[73] was utilized. The 'reslice' tool and 'average projection filter' were applied to generate the kymographs. To create each kymograph 10-50 slices were used to generate the average projection. Line profiles, wavelet analysis, Fast-Fourier Transformation, auto-correlation, cross-correlation, average peaks and interpeak intervals plots were performed using MATLAB. For the determination of interpeak interval, individual peaks were identified based on secondary derivatives. The individual peaks were aligned at peak positions, and average curves were generated to obtain rise and drop phases. To investigate the occurrence of a period-doubling bifurcation, a return map was generated by plotting the interpeak interval (P1) relative to the next interpeak interval (P+1). Custom codes used for analysis are deposited on Github (https://github.com/min-wu-lab/mmo-analysis, https://doi.org/10.5281/zenodo.8083400) and is publicly available.

Statistical analysis

Statistical analysis were performed using GraphPad Prism9. To compare cell size changes between wild type, E-Syt1 KD and E-Syt1/INPP4B DKD, unpaired two-tailed student t-test were used. Data were shown as mean ± SD. Please refer to figures and figure legends for number of cells used for quantification per condition.